Morphology and Crystallinity Effects of Nanochanneled Niobium Oxide Electrodes for Na-Ion Batteries

Cyrus Koroni,* Kiev Dixon, Pete Barnes, Dewen Hou, Luke Landsberg, Zihongbo Wang, Galib Grbic', Sarah Pooley, Sam Frisone, Tristan Olsen, Allison Muenzer, Dustin Nguyen, Blayze Bernal, and Hui Xiong*
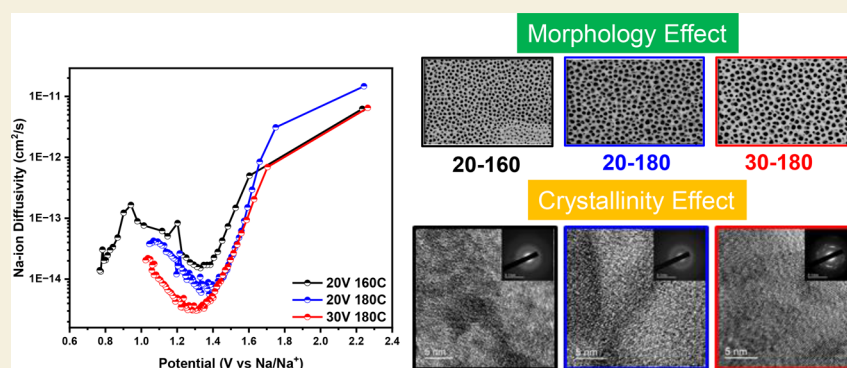
Cite This: https://doi.org/10.1021/acsnanoscienceau.3c00031

Read Online

| ACCESS | | Metrics & More | | Article Recommendations | | Supporting Information |

ABSTRACT: Niobium pentoxide (Nb_2O_5) is a promising negative electrode for sodium ion batteries (SIBs). By engineering the morphology and crystallinity of nanochanneled niobium oxides (NCNOs), the kinetic behavior and charge storage mechanism of Nb_2O_5 electrodes were investigated. Amorphous and crystalline NCNO samples were made by modulating anodization conditions (20−40 V and 140−180 °C) to synthesize nanostructures of varying pore sizes and wall thicknesses with identical chemical composition. The electrochemical energy storage properties of the NCNOs were studied, with the amorphous samples showing better overall rate performance than the crystalline samples. The enhanced rate performance of the amorphous samples is attributed to the higher capacitive contributions and Na-ion diffusivity analyzed from cyclic voltammetry (CV) and the galvanostatic intermittent titration technique (GITT). It was found that the amorphous samples with smaller wall thicknesses facilitated improved kinetics. Among samples with similar pore size and wall thickness, the difference in their power performance stems from the crystallinity effect, which plays a more significant role in the resulting kinetics of the materials for Na-ion batteries.

KEYWORDS: nanochanneled niobium oxides, morphology effect, crystallinity effect, sodium ion batteries, charge storage and transport, negative electrode materials

INTRODUCTION

Since its commercialization by Sony in 1991, the lithium-ion battery (LIB) has been implemented into mobile devices, electric vehicles, and grid storage.[1] However, with the continuously increasing cost of lithium raw materials from the booming market of electric vehicles and the finite resource of lithium in the Earth's crust, an alternative option in sodium-ion batteries (SIBs) may provide lower cost and sustainability.[2−4] SIBs fundamentally operate in the same manner as LIBs, and the increased availability and lower raw material costs and operational costs due to not exclusively requiring copper current collectors make SIBs a very attractive alternative. Additionally, with the increase in renewable energy, the utilization of SIBs for grid energy storage systems becomes increasingly optimiztic. Currently, hard carbon is the most popular negative electrode material used for SIBs with good

specific capacity,[5] as well as stable cycling,[6] and is thus regarded as the most promising negative electrode material candidate for SIBs.[7] Despite that, hard carbon is plagued with poor rate performance, safety concerns, and poor initial irreversible capacity.[7−9] The low operation potential of hard carbon overlaps with the place where Na dendritic formation may occur, possibly leading to a short circuit and thermal runaway. Other materials such as alloy-based and conversion-type negative electrodes including Sn, Sb, Ge, Bi, and P all

A

promise high theoretical capacities though they encounter issues with volume expansion and pulverization.[9]

Niobium oxides have been studied as negative electrodes in enhanced electrochemical storage systems for their stability and are an exciting option for SIBs.[10−15] Nb_2O_5 negative electrodes have a higher intercalation potential than hard carbon, preventing them from suffering from sodium plating and thermal runaway. A wide variety of polymorphs exist for Nb_2O_5 including orthorhombic, pseudohexagonal, and monoclinic phases, making them a material with a broad range of tunability.[16] Kim et al. were the first to report Nb_2O_5 electrodes for SIBs and proposed that a nanoporous Nb_2O_5/carbon composite could function as a promising Na^+ insertion material.[17] This composite demonstrated a reversible capacity of 175 mAh/g for up to 300 cycles, which was attributed to facile Na-ion and electron transport as well as a large interface area with good electrolyte penetration. There have been a few other works, many of which focused on the pseudocapacitive behaviors of Nb_2O_5 coated with carbon.[18−26] The good electrical properties of carbon can help the wide band gap Nb_2O_5 material overcome its low intrinsic electrical conductivity. Little work has been done to systematically investigate the morphology and crystallinity effects on the electrochemical properties of the Nb_2O_5 electrodes for SIBs.

Molten Na reduced orthorhombic Nb_2O_5($T-Nb_2O_5$) nanorods were reported with enhanced sodium storage, rate performance, and diffusion kinetics attributed to oxygen vacancies.[27] The $T-Nb_2O_5$ nanorod electrode delivered a capacity of 100.7 mAh/g at 1C rate and 44.1 mAh/g at 5C rate following 1000 cycles. It was suggested that the amorphous boundary induced by the oxygen vacancies can provide more active sites and improve the capacitive contribution.[27] Work by Ni et al. highlighted the benefit of amorphous Nb_2O_5 in addition to the generation of oxygen vacancies by hydrogenation.[28] The amorphous Nb_2O_5 electrodes exhibited a capacity of 185 mAh/g at a rate of 0.5 C and an impressive reversible capacity of 133 mAh/g at a 2 C rate, although the authors did not discuss the charge storage mechanism related to their findings. Another work by Zhang et al. on amorphous Nb_2O_5 electrodes in a 3D ordered microporous structure exhibited a reversible capacity of 197 mAh/g at a current density of 0.1 A/g for over 100 cycles.[29] The highly porous structure was credited for good penetration of electrolyte and the acquisition of high-power density that led to the improved performance, underscoring the importance of morphology for the uptake of electrolyte and increased electrochemical performance of Nb_2O_5. As a wide band gap n-type semiconductor, Nb_2O_5 suffers from poor electrical conductivity. Methods for tackling the poor electrical conductivity include utilizing different polymorphs[30,31] and creating nanoarchitecture to improve electrical conductivity. Though there have been studies with Nb_2O_5 as negative electrode materials in SIBs, many of them utilize carbon to improve electrical conductivity while there are few modifying the nanostructure of these materials. The connection between morphology, structure, and electrochemical performance has seldom been discussed in literature. Tunable control of the nanostructure of Nb_2O_5 would allow for the optimization of materials for use in electrochemical energy storage systems.

Herein, we investigate the morphology and crystallinity effects on nanochanneled niobium oxide (NCNO) negative electrode materials for SIBs. Our work focuses on the optimization of the morphology and crystallinity of electrochemically anodized NCNOs without the use of additives or conductive agents. Amorphous and crystalline NCNOs were prepared with identical chemical compositions but differing pore sizes and wall thicknesses. The crystallinity was analyzed via X-ray diffraction (XRD) and transmission electron microscopy (TEM). The pore sizes and wall thicknesses were studied via scanning electron microscopy (SEM). We found that the electrochemical performance in terms of rate capability directly relates to the pore size, wall thickness, and crystallinity of the anodized NCNOs where amorphous samples with larger pore sizes and smallest wall thicknesses exhibit higher capacity. The charge storage and transport mechanisms in NCNO were investigated via cyclic voltammetry (CV) and galvanostatic intermittent titration technique (GITT) to provide further insight into the kinetic behavior of the amorphous and crystalline samples.

■ MATERIALS AND METHODS

Synthesis

NCNO samples were prepared via electropolishing, followed by electrochemical anodization. Electropolishing was conducted following the method[32] established by our group with slight modifications described herein. Samples of niobium metal (0.127 mm, Alfa Aesar, 99.8%) were cleaned by sonication in acetone, isopropanol, and deionized water for 5 min each and then dried with compressed air. Clean samples were taped on the back and electropolished in a solution of 10% sulfuric acid in methanol (Fisher) in a two-electrode cell with Nb foil as the working and counter electrode. The solution was chilled to −70 °C in a bath of acetone and dry ice. Samples were placed in the solution and connected to a BK precision 9206 power supply. A constant potential of 20 V − 25 V was applied and maintained for 2 h. To conclude the polishing process, the foils were removed from the solution, washed with deionized water, and then sonicated for 5 min in deionized water.

NCNOs were prepared by electrochemical anodization of electropolished Nb metal, using a method adopted from the work by Schmuki et al.[33] The electropolished Nb metal was taped on the back and outer front edges, excluding the top to help even current distribution. Niobium oxide films were formed by anodization in a 10 wt % dibasic potassium phosphate (K_2HPO_4) in glycerol solution, with a Pt mesh as a counter electrode. Anodization potential and temperature were varied from 20 to 40 V in 10 V increments and from 140 to 180 °C in 20 °C increments, respectively. The temperature was controlled using a heated stir plate with a temperature sensing probe. After anodization, the tape was removed and samples were sonicated for 5 min in deionized water. The samples were then placed in a vacuum oven at 80 °C overnight. Samples will be denoted in the form of 20 V160C for an anodization voltage of 20 V and a temperature of 160 °C, respectively.

Physical Characterization

Prior to SEM imaging, samples were ion-milled to expose the underlying pore structure. Ion-milling was conducted by using a Veeco ME 1001 Ion Beam Milling System. Samples were milled at a 90° incident angle for 5 min. The accelerating beam voltage was 549 eV. Beam current was set to 298 mA and the cathode current was 56.7 A. SEM was performed by using a Field Emission FEI (Teneo) FESEM system. Images were collected using the T1 detector with 50 pA current and an accelerating voltage of 10 kV. X-ray diffractions were performed on a Rigaku Miniflex 600 benchtop X-ray diffractometer. Samples were analyzed with an angular range from 10° to 80°, at a rate of 3° per min and a step size of 0.01°. TEM measurements were performed on a JEOL JEM-2100F instrument with an acceleration voltage of 200 kV. The materials for TEM were scraped and collected from the thin film samples, which were directly dispersed on a Cu grid.
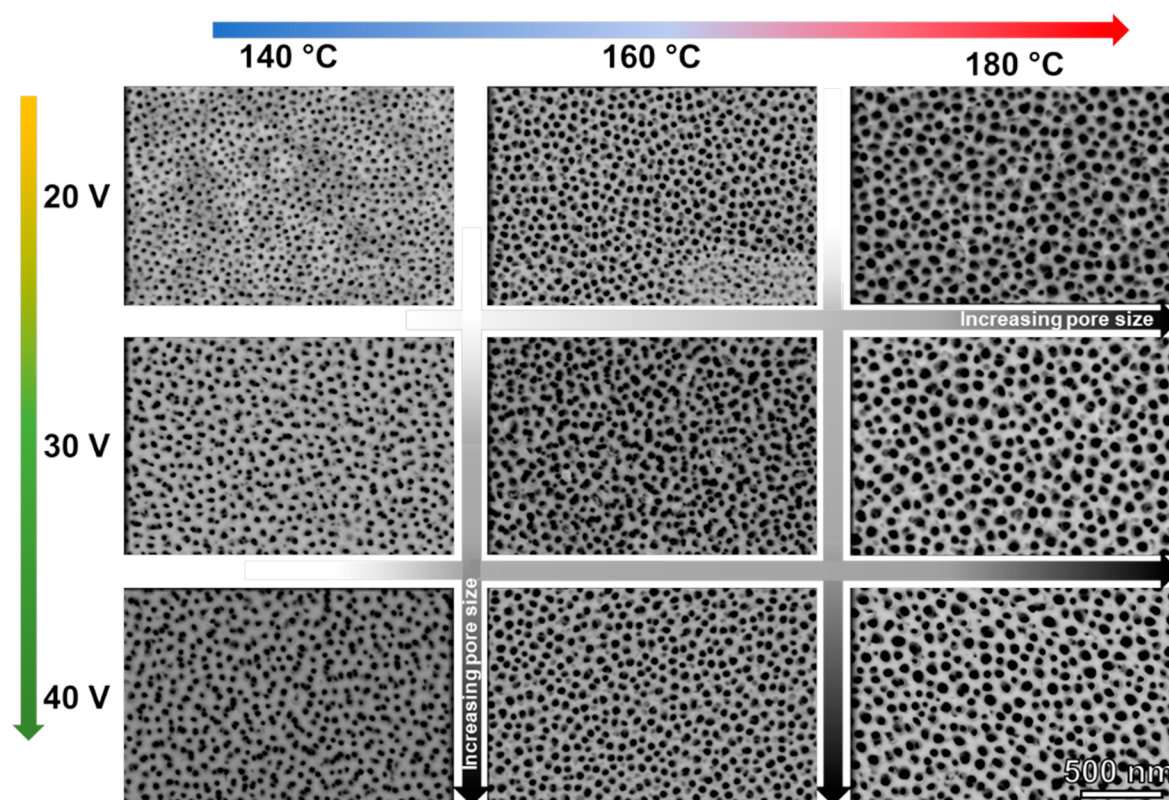
Figure 1. Top-view SEM images of NCNOs formed under varying temperatures and voltages during anodization.

Electrochemical Characterization

Coin cells were constructed by cutting samples into 15 mm diameter disks with an EQ-T06 Disk (MTI, Co) die cutter. Cells were constructed into coin-type half cells in an argon filled glovebox, where O_2 levels were maintained below <0.5 ppm. Sodium metal counter electrode material was purchased from Aldrich. The electrolyte used was 1 M $NaClO_4$ (Alpha Aesar) in ethylene carbonate (EC)/ propylene carbonate (PC) (1:1 volume ratio) (BASF) with 2% fluoroethylene carbonate (FEC). Whatman 2325 glassy fiber separators were used. Cells were cycled galvanostatically on a LAND CT2001A, with a potential window between 0.6 and 2.5 V vs Na/Na^+ with a 10 min relaxation time between cycles. Three-electrode cells (EL-CELL, ECC-ref cell) were made with NCNO 15 mm working electrodes and Na metal counter and reference electrode. GITT was completed with an applied current of 30 μA for 30 min followed by a 2 h relaxation to approach steady state. Cyclic voltammograms were obtained between potentials 0.6 and 2.5 V at scan rates of 0.1, 0.2, 0.5, 1, 2, 5, and 10 mV/s.

Active Material Mass and Film Thickness Measurements

As-formed disks of niobium metal with NCNO on the surface were weighed prior to cell construction. After cycling, the disks were etched in a solution of 2.5% HF (Acros) in 12 M HCl (Fisher) solution to remove the oxide layer. The mass of the active material was then determined by the difference of the samples before and after etching. The loading density of the electrodes is 1.9 ± 1.0 mg/cm^2. The film thickness was measured by inspection of the cross sections using SEM.

■ RESULTS AND DISCUSSION

Pore Size and Wall Thickness Analysis

NCNO samples were prepared via electrochemical anodization by altering the voltage between 20 and 40 V and the temperature between 140 and 180 °C. A strong correlation exists between the resulting nanostructure and the conditions of anodization voltage and temperature (Figure 1).

A voltage and temperature threshold are required to form the nanochanneled architecture, as shown in Figure S1 (Supporting Information). Anodization with voltages less than 10 V yielded sponge-like oxide films while at temperatures lower than 140 °C well-defined pores were not formed. When the anodization voltage and temperature were increased to 20 V and 140 °C, samples began to form a porous structure (Figure 1), albeit with relatively small pores (~27.0 nm) and a large wall thickness (~35 nm). Pore sizes and wall thicknesses for varied voltages and temperatures are summarized in Table 1. At 20 V and 140 °C the surface pores account for only ~14.3% of the surface area. It was found that by increasing the anodization temperature while keeping the voltage constant (20 V) a 32% increase of pore size was seen at a temperature of 160 °C. As the anodization temperature was further increased

Table 1. Anodization Conditions and the Resulting Pore Features of NCNOs

potential (V)	temperature (°C)	avg pore diameter ± std dev (nm)	avg wall thickness ± std dev (nm)	pore area (% of surface area)
20	140	27.0 ± 6.9	32.7 ± 8.0	14.3
30	140	32.9 ± 7.8	31.8 ± 13.9	13.6
40	140	33.2 ± 8.3	29.0 ± 14.5	15.3
20	160	35.7 ± 8.8	21.9 ± 8.0	21.1
30	160	36.6 ± 11.8	22.9 ± 9.0	20
40	160	40.2 ± 7.4	24.2 ± 10.6	22.6
20	180	47.2 ± 13.3	27.8 ± 16.5	23.8
30	180	51.8 ± 13.4	32.2 ± 12.8	23.4
40	180	47.4 ± 14.0	37.0 ± 15.9	21.8

to 180 °C there was another 32% increase in pore size to 47.2 nm, showing a direct correlation of pore size and anodization temperature. At 20 V180 °C the pores account for ∼24% of the surface area, showing an overall increase in the porosity of the nanostructured material. Similar results were seen when anodizing samples at 30 and 40 V, respectively, where initial pore sizes were shown to increase in size when anodization occurred at higher temperatures (Figure 1 and Table 1).

Anodization voltage effect was evaluated by keeping the temperature constant while varying voltages from 20 to 40 V. A similar result of an increased pore size was observed. It is noted that the voltage effect on anodization is not as effective in increasing the pore size as the temperature, demonstrating a higher dependency of the anodization pore size to temperature conditions. Higher anodization temperatures allow for faster kinetics, and reactions to occur spontaneously. Our results agree well with prior work on pore size dependence of anodization temperature and voltage.[33] The average wall thickness seems to have a more correlated relationship with both the voltage and temperature. Generally, anodization at 160 °C and lower voltages promotes smaller walls. Smaller walls are beneficial for faster charge transport with NCNO electrodes.

The structure of nanochanneled Nb_2O_5 was investigated by XRD to determine the crystallinity of the anodized samples (Figure 2). Samples anodized at 20 V displayed a broad hump
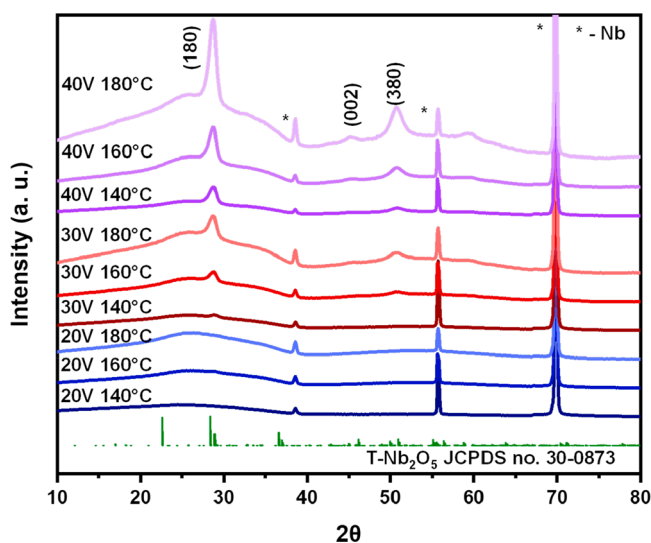

Figure 2. XRD of anodically grown NCNOs at different voltages and temperatures. *Peaks from the Nb substrate.

from 10° - 40°, which is indicative of an amorphous structure. When the anodization voltage was increased to 30 V, peaks emerge at 28.5° and 50.8°, which can be well indexed to the orthorhombic $T\text{-}Nb_2O_5$ (JCPDS 30−0873) phase with the space group of *Pbam*. The peaks near 28.5° are convoluted including (180) and (200) planes. The peaks located at 46.8° and 50.8° correspond to the (002) and (380) planes, respectively. At 40 V, the peaks of the samples become sharper, which suggests the gradual increase of the crystallite size and extent of the crystallization. Notably, the (001) plane near 25° does not appear for all crystalline samples due to the preferential orientation of the thin films grown on a textured Nb substrate.

Temperature was also shown to promote the crystallinity of the samples. As the temperature and voltage are increased, the peaks become sharper and more pronounced. The peak narrowing is indicative of grain growth within the material. Using the Scherrer equation, the crystallite sizes in the crystalline samples may be estimated.[34,35] Crystallite sizes were calculated to be 2.1, 2.8, 4.4, 4.5, and 5.2 nm for the 30−160, 30−180, 40−140, 40−160, and 40−180 samples using the Scherrer equation, respectively. These results underscore that both voltage and temperature play a role in the degree of crystallinity, but voltage is more critical. A voltage threshold (e.g., >30 V) needs to be met before temperature can take effect on crystallization as under all voltages below 30 V the samples display no crystallinity.

The structure of select NCNOs at conditions 20V160C (20−160), 20V180C (20−180), and 30V180C (30−180) was further investigated by TEM. The degree of ordering of the samples was examined by high resolution TEM (HRTEM) and selected area electron diffraction (SAED) shown in Figure 3. The lack of pronounced lattice fringes (Figure 3d, e) and the characteristic diffuse rings in SAED (Figure 3a, b) suggest that the 20−160 and 20−180 samples are both amorphous. For the 30−180 sample, there are distinct grains in the HRTEM (Figure 3f) suggesting its crystalline feature. The SAED pattern shows diffraction rings attributed to the $T\text{-}Nb_2O_5$ structure. It is noted that the (001) diffraction, which is missing in XRD of the 30−180 sample, appears in the SAED. We believe that the preferred orientation present in the NCNOs when on the substrate disappears when we prepared the TEM sample. Our preparation includes scratching the surface of the NCNOs and then applying the sample to the grid. This eliminates the texturing, allowing for the (100) plane to appear in the electron diffraction.

Electrochemical Performance

To investigate the morphology and crystallinity effect, select samples (20 and 30 V) were evaluated. The rate capability of the electrodes is shown in Figure 4. At low rates, the amorphous samples (20−160, 20−180) demonstrate enhanced capacity over their crystalline counterparts at ∼117 and ∼115 mAh/g under a current density of 8 mA/g, respectively. As the rates increased, their overall performance still surpassed those of the other samples. The 20−140 amorphous sample initially demonstrates good performance at low rates of 8 and 16 mA/g current densities, though as the rate increases a dramatic drop is seen starting from 80 mA/g, and at 400 mA/g it shows the lowest capacity. The modified Peukert plot (Figure 4b) is helpful to compare the rate performance among samples, which is as follows: 20−160 (amorphous) > 20−180 (amorphous) > 30−160 (partially crystalline) > 30−140 (partially crystalline) > 30−180 (crystalline) > 20−140 (amorphous). The general trend is that high crystallinity leads to worse rate performance with 20−140 as an exception. Among samples with similar crystallinity, it is seen that wall thickness plays a key role in the kinetics of the electrodes. For example, among the amorphous samples, 20−160 electrode shows the best rate capability with the smallest wall thickness (21.9 ± 8.0 nm) while among the partial crystalline samples, the 30−160 electrode has better rate due to smaller wall thickness (22.9 ± 9.0 nm). The results suggest that smaller walls can reduce the transport distance for both Na^+ ions and electrons to facilitate faster kinetics. For the crystalline 30−180 sample, it shows the worst initial capacity, while maintaining
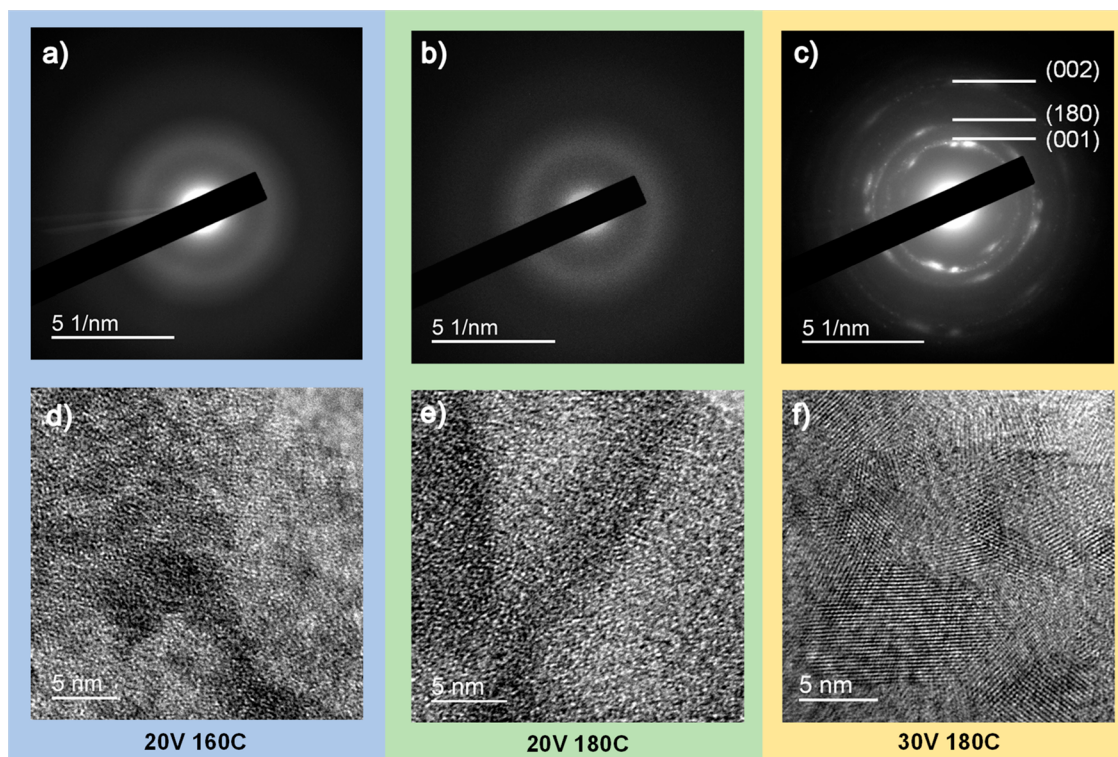
Figure 3. TEM images of anodically grown NCNOs. (a−c) selected area electron diffraction (SAED) and (d−f) high-resolution TEM (HRTEM) of 20−160, 20−180, and 30−180, respectively.
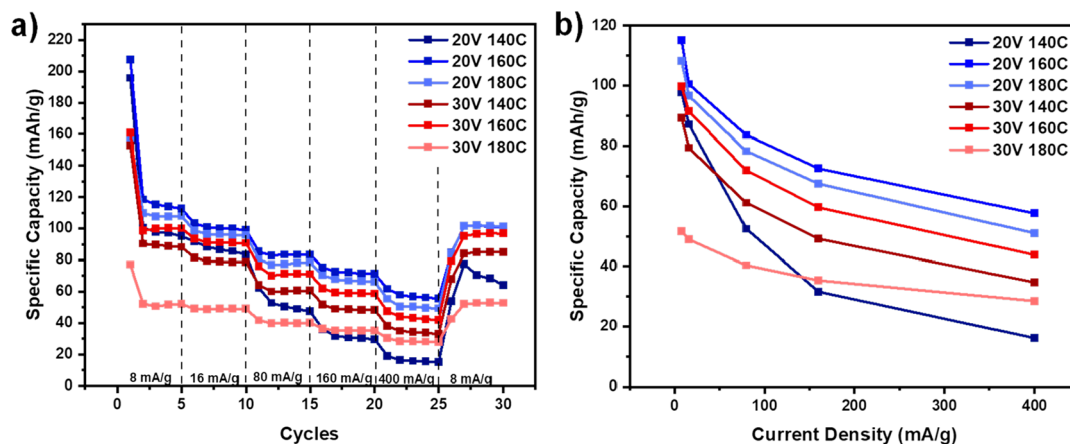

Figure 4. (a) Rate capabilities of NCNO electrodes and rate capability and (b) modified Peukert plot. All samples were cycled between 0.6 and 2.5 V.

good capacity retention at higher rates. This indicates that increased crystallinity may lead to decreased sites for charge storage. Lastly, the poor rate capability of the 20−140 sample can be explained by its smallest pore size (∼27 nm) and large wall thickness (∼33 nm). Smaller pores make it difficult for electrolyte penetration, which increases the time for charge transport.

An intriguing point of discussion emerges from the poor rate capability of the 20−140 sample, attributable to its notably small pore size (approximately 27 nm) and significant wall thickness (∼ 33 nm). The impact of the wall thickness on rate capacity is especially noteworthy. The considerable thickness impairs ion transport within the sample, in turn, compromising the rate capacity. Furthermore, the smaller pores present challenges for electrolyte penetration, further exacerbating the

charge transport kinetics. However, it is crucial to consider the relative influence of the pore size and wall thickness on these outcomes. A potential question that might arise from this study is the precise effect of the pore size on electrolyte penetration. While the small pore size undeniably affects the access of the electrolyte, we postulate that the dramatic differences observed here are more likely predominantly driven by wall thickness rather than pore size.

Additionally, the thickness of the samples was considered. It is noted that the 30−180 sample is the thickest (17.3 μm) among all samples, which partially explains its low capacity due to slow electron transport from the current collector to the top of the nanochannels, especially at high rates. However, the thickness is not considered the major cause of the inferior rate performance seen in crystalline samples as explained next. 40−
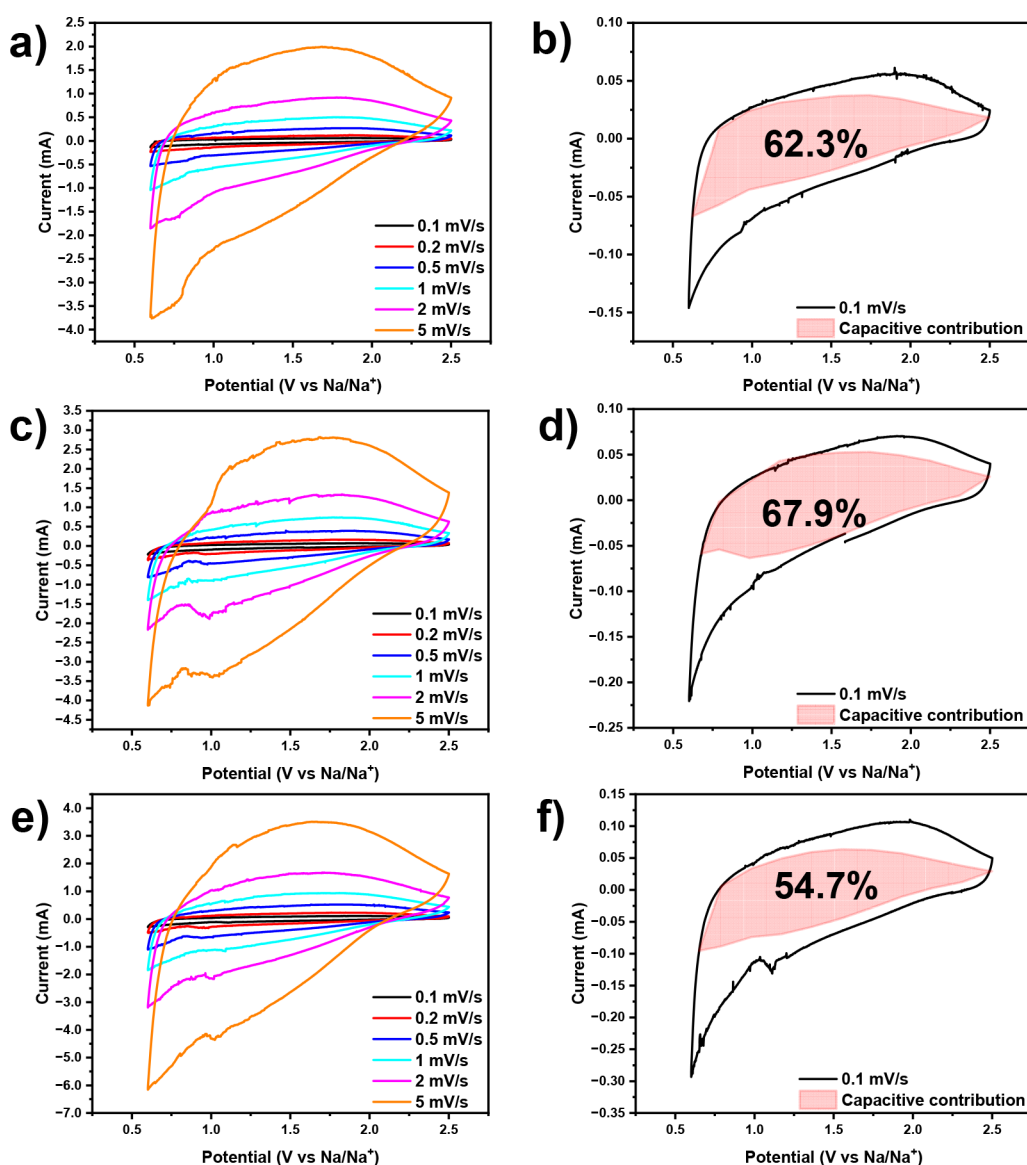
Figure 5. (a, c, e) CV curves of the 20−160, 20−180, and 30−180 electrodes at various scan rates and (b, d, f) voltammetric response of the 20−160, 20−180, and 30−180 samples at the scan rate of 0.1 mV/s, respectively.

160 sample which has similar film thickness ($\sim$ 8.98 μm) and wall thickness with 20−160 sample (amorphous, 9 μm) but high crystallinity was evaluated (Figure S3, Supporting Information). A stark contrast in the rate capability is evident. Specifically, the 40−160 sample exhibits significantly poorer power performance as compared with the 20−160 sample. Despite the anticipated improvement in electronic conductivity due to higher crystallinity in the 40−160 sample as compared to amorphous samples, the better power performance of the 20−160 sample is attributed to the enhanced Na diffusivity. In addition, the increased crystallinity of the 40−160 sample as compared to the 30−160 sample leads to worse rate capability although the 40−160 sample has a similar wall thickness and smaller film thickness compared to the 30−160 sample (14.1 μm), further confirming our hypothesis that higher crystallinity leads to worse rate capability.

Electrochemical Charge Storage and Transport Mechanisms

The differences in electrochemical performance found between the amorphous and the crystalline samples indicate that there may be a different mechanism for the charge storage and transport processes in the NCNOs. Three samples (20−160, 20−180, and 30−180) were further investigated to understand the relationship between morphology, crystallinity, and the charge storage mechanism. The morphology effect is assessed on 20−160 and 20−180 samples, which are both amorphous with varying pore size and wall thickness. The crystallinity effect is evaluated on 20−180 and 30−180 samples, which have similar morphology by varying crystallinity. Cyclic voltammetry at different scan rates of 0.1, 0.2, 0.5, 1, 2, and 5 mV/s was conducted on the three electrodes (Figure 5a, c, and e) to investigate the charge storage mechanism which can be analyzed according to the power law relationship.[36]
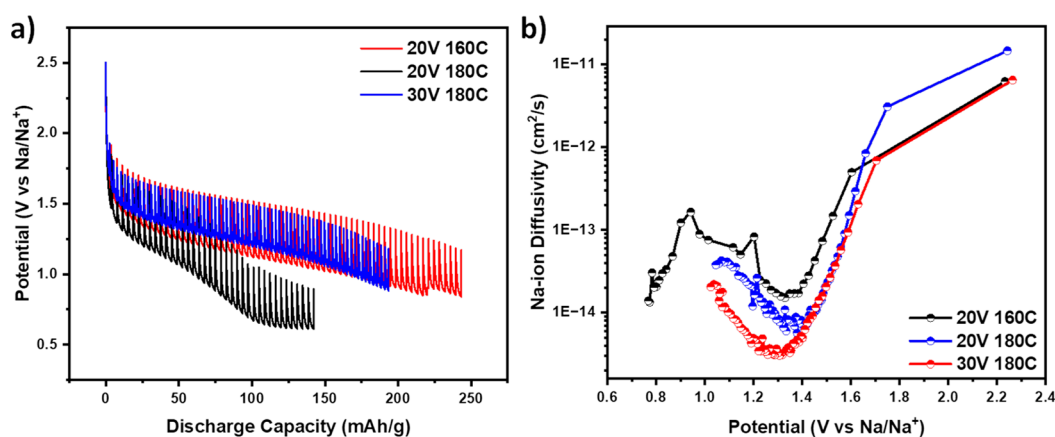
$$i = av^b \tag{1}$$

Figure 6. (a) GITT and (b) Na$^+$ diffusivity vs voltage of the 20−160, 20−180, and 30−180 electrodes.

where i is the current, v is the scan rate, a and b are the adjustable parameters. The b-values may be found from the slope of the plot of log i vs log v where the b-value has two well-defined conditions: $b = 0.5$ and $b = 1.0$. For $b = 0.5$, the current is proportional to the square root of the scan rate, v, and indicates diffusion-limited intercalation. For $b = 1.0$, the current is proportional to the scan rate, v, and indicates surface capacitive processes. The b-values for the 20−160, 20−180, and 30−180 samples are plotted in Figure S2 (Supporting Information). The 20−160 and 20−180 samples both had similar b-values ranging from 0.8−0.9 in the potential range from 1.5 to 2.5 V. Below those potentials the 20−160 sample maintained higher b-values than both 20−180 and 30−180 samples indicating that it involved in more surface capacitive processes.

To better understand the quantitative contribution of the diffusion-limited intercalation process and pseudocapacitive process, the capacitive contribution (shaded region) for 20−160, 20−180, and 30−180 samples during Na$^+$ insertion are shown in Figure 5 according to the equation:[37,38]

$$i(v) = k_1 v + k_2 v^{1/2} \qquad (2)$$

This equation may be rearranged to

$$\frac{i(v)}{v^{1/2}} = k_1 v^{1/2} + k_2 \qquad (3)$$

where $k_1 v$ and $k_2 v^{1/2}$ correspond to the current contributions from the surface capacitive processes and the diffusion-controlled intercalation process, respectively. Determination of k_1 and k_2 may be found by plotting $\frac{i(v)}{v^{1/2}}$ vs $v^{1/2}$ and finding the slope and intercept, respectively. The charge storage mechanism can then be investigated by quantitatively looking at the fraction of $k_1 v$ and $k_2 v^{1/2}$. The CV curves of the 20−160, 20−180, and 30−180 electrodes at slow scan rate of 0.1 mV/s are shown in Figure 5b, d, and f, respectively, where the shaded area indicates the capacitive contribution to the charge storage. The capacitive contributions of the 20−160, 20−180, and 30−180 electrodes are 62.3%, 67.9%, and 54.7%, respectively.

The increased capacitive contributions for the 20−160 and 20−180 samples over the 30−180 sample agree well with their rate capability discussed earlier. This lower capacitive contribution of the crystalline 30−180 sample suggests that the sample relies more upon diffusion-limited charge storage, which possesses slower kinetics. Though the increased pore

size and decreased wall thicknesses of the 30−180 sample almost match the 20−180 sample and exceed the 20−160 sample, the lower capacitive contribution due to crystallinity prevents the crystalline sample from having the improved capacity as the amorphous samples under the same rates. The capacitive contribution of the three samples suggests that crystallinity has a more significant effect in the kinetics of charge storage in NCNOs compared to the nanostructure morphology.

We then conducted GITT (Figure 6) of the NCNO samples to evaluate the Na$^+$ diffusivity in the amorphous and crystalline samples.[39] The diffusion coefficient as a function of the potential for the insertion of Na$^+$ ions into the NCNOs is shown in Figure 6b. The Na$^+$ diffusivities of the 20−160 sample were higher than those of the 20−180 and 30−180 samples for the potential range below 1.8 V and beyond 1.8 V, 20−180 begins to outperform the other two. All three samples show a dip of diffusivity around 1.3−1.4 V, which indicates formation of reaction intermediates/phase transformation during Na$^+$ intercalation that impedes the ion diffusion. The trend of the Na$^+$ diffusivity corroborates well with the rate capability results and underscores the importance to modulate crystallinity and morphology in NCNOs for improving charge transport kinetics.

■ CONCLUSION

NCNOs were electrochemically anodized under various conditions to produce samples with varying pore sizes, wall thicknesses, and crystallinity. A strong relationship between the voltage and temperature with the pore size, wall thickness, and crystallinity was found. The anodization temperature of the NCNOs shows a greater effect on regulating pore size and wall thicknesses, while the anodization voltage plays a key role in controlling the crystallinity of the samples. The rate performance of NCNO electrodes shows that amorphous samples outperform the crystalline samples, while larger pores and smaller wall thickness promote better kinetics among samples of the same crystallinity. The charge storage and transport mechanisms in NCNO electrodes are further investigated with CV and GITT. Both amorphous 20−160 and 20−180 samples demonstrated higher capacitive contributions than the crystalline 30−180 sample, conductive to their better rate performance. Among the amorphous samples, larger pores and smaller wall thickness facilitate a higher capacitive contribution for better charge storage kinetics. The diffusivity obtained from

the GITT further shows the improved performance of the 20−160 sample over the 20−180 and the 30−180 samples, which suggests the influence of both morphology and crystallinity in charge transport kinetics. Moreover, the similarity in the pore size and wall thickness of the 20−180 and 30−180 samples suggests the difference in their power performance is rooted from crystallinity effect, and it plays a more significant role in the kinetics of the NCNO electrodes.

■ ASSOCIATED CONTENT

ⓢ Supporting Information

The Supporting Information is available free of charge at https://pubs.acs.org/doi/10.1021/acsnanoscienceau.3c00031.

> SEM images of electrochemically anodized niobium oxides under different voltages and temperatures; *b*-values of the 20−160, 20−180, and 30−180 samples; rate performance of the 20−160, 20−180, 30−160, and 40−160 NCNO samples; description of GITT analysis (PDF)

■ AUTHOR INFORMATION

Corresponding Authors

Hui Xiong − *Micron School of Materials Science & Engineering, Boise State University, Boise, Idaho 83725, United States;* ⓞ orcid.org/0000-0003-3126-1476; Email: clairexiong@boisestate.edu

Cyrus Koroni − *Micron School of Materials Science & Engineering, Boise State University, Boise, Idaho 83725, United States;* Email: cyruskoroni@u.boisestate.edu

Authors

Kiev Dixon − *Micron School of Materials Science & Engineering, Boise State University, Boise, Idaho 83725, United States*

Pete Barnes − *Micron School of Materials Science & Engineering, Boise State University, Boise, Idaho 83725, United States; Energy Storage and Electric Vehicle Department, Idaho National Laboratory, Idaho Falls, Idaho 83401, United States*

Dewen Hou − *Micron School of Materials Science & Engineering, Boise State University, Boise, Idaho 83725, United States; Center for Nanoscale Materials, Argonne National Laboratory, Lemont, Illinois 60439, United States*

Luke Landsberg − *Micron School of Materials Science & Engineering, Boise State University, Boise, Idaho 83725, United States*

Zihongbo Wang − *Micron School of Materials Science & Engineering, Boise State University, Boise, Idaho 83725, United States*

Galib Grbic' − *Micron School of Materials Science & Engineering, Boise State University, Boise, Idaho 83725, United States*

Sarah Pooley − *Micron School of Materials Science & Engineering, Boise State University, Boise, Idaho 83725, United States*

Sam Frisone − *Micron School of Materials Science & Engineering, Boise State University, Boise, Idaho 83725, United States*

Tristan Olsen − *Micron School of Materials Science & Engineering, Boise State University, Boise, Idaho 83725, United States*

Allison Muenzer − *Micron School of Materials Science & Engineering, Boise State University, Boise, Idaho 83725, United States*

Dustin Nguyen − *Micron School of Materials Science & Engineering, Boise State University, Boise, Idaho 83725, United States*

Blayze Bernal − *Micron School of Materials Science & Engineering, Boise State University, Boise, Idaho 83725, United States*

Complete contact information is available at:
https://pubs.acs.org/10.1021/acsnanoscienceau.3c00031

Author Contributions

CRediT: **Cyrus Koroni** data curation, formal analysis, investigation, validation, visualization, writing-original draft, writing-review & editing; **Kiev Dixon** data curation, formal analysis, investigation, visualization; **Pete Barnes** data curation, formal analysis, investigation, visualization, writing-original draft; **Dewen Hou** data curation, formal analysis, visualization, writing-review & editing; **Luke Landsberg** data curation, investigation; **Zihongbo Wang** data curation, investigation; **Galib Grbic'** data curation, investigation; **Sam Frisone** data curation, investigation; **Sarah Pooley** data curation, investigation; **Tristan Olsen** data curation, investigation; **Allison Muenzer** data curation, investigation; **Dustin Nguyen** data curation, investigation; **Blayze Bernal** investigation; **Hui Xiong** conceptualization, formal analysis, funding acquisition, investigation, methodology, project administration, supervision, visualization, writing-original draft, writing-review & editing.

Notes

The authors declare no competing financial interest.

■ ACKNOWLEDGMENTS

■ REFERENCES

(1) Grey, C. P.; Hall, D. S. Prospects for Lithium-Ion Batteries and beyond—a 2030 Vision. *Nat. Commun.* **2020**, *11* (1), 6279.

(2) Kubota, K.; Dahbi, M.; Hosaka, T.; Kumakura, S.; Komaba, S. Towards K-Ion and Na-Ion Batteries as "Beyond Li-Ion. *Chem. Rec.* **2018**, *18* (4), 459−479.

(3) Li, J.; Du, Z.; Ruther, R. E.; AN, S. J.; David, L. A.; Hays, K.; Wood, M.; Phillip, N. D.; Sheng, Y.; Mao, C.; Kalnaus, S.; Daniel, C.; Wood, D. L. Toward Low-Cost, High-Energy Density, and High-Power Density Lithium-Ion Batteries. *JOM* **2017**, *69* (9), 1484−1496.

(4) Usiskin, R.; Lu, Y.; Popovic, J.; Law, M.; Balaya, P.; Hu, Y.-S.; Maier, J. Fundamentals, Status and Promise of Sodium-Based Batteries. *Nat. Rev. Mater.* **2021**, *6* (11), 1020−1035.

(5) Wang, P.-F.; You, Y.; Yin, Y.-X.; Guo, Y.-G. Layered Oxide Cathodes for Sodium-Ion Batteries: Phase Transition, Air Stability, and Performance. *Adv. Energy Mater.* **2018**, *8* (8), 1701912.

(6) Qiu, S.; Xiao, L.; Sushko, M. L.; Han, K. S.; Shao, Y.; Yan, M.; Liang, X.; Mai, L.; Feng, J.; Cao, Y.; Ai, X.; Yang, H.; Liu, J. Manipulating Adsorption−Insertion Mechanisms in Nanostructured Carbon Materials for High-Efficiency Sodium Ion Storage. *Adv. Energy Mater.* **2017**, *7* (17), 1700403.

(7) Chen, X.; Zheng, Y.; Liu, W.; Zhang, C.; Li, S.; Li, J. High-Performance Sodium-Ion Batteries with a Hard Carbon Anode: Transition from the Half-Cell to Full-Cell Perspective. *Nanoscale* **2019**, *11* (46), 22196−22205.

(8) Nayak, P. K.; Yang, L.; Brehm, W.; Adelhelm, P. From Lithium-Ion to Sodium-Ion Batteries: Advantages, Challenges, and Surprises. *Angew. Chem., Int. Ed.* **2018**, *57* (1), 102−120.

(9) Zhang, W.; Zhang, F.; Ming, F.; Alshareef, H. N. Sodium-Ion Battery Anodes: Status and Future Trends. *EnergyChem* **2019**, *1* (2), No. 100012.

(10) Viet, A. L.; Reddy, M. V.; Jose, R.; Chowdari, B. V. R.; Ramakrishna, S. Nanostructured Nb$_2$O$_5$ Polymorphs by Electrospinning for Rechargeable Lithium Batteries. *J. Phys. Chem. C* **2010**, *114* (1), 664−671.

(11) Yan, L.; Rui, X.; Chen, G.; Xu, W.; Zou, G.; Luo, H. Recent Advances in Nanostructured Nb-Based Oxides for Electrochemical Energy Storage. *Nanoscale* **2016**, *8* (16), 8443−8465.

(12) Schäfer, H.; Gruehn, R.; Schulte, F. The Modifications of Niobium Pentoxide. *Angew. Chem., Int. Ed. Engl.* **1966**, *5* (1), 40−52.

(13) Lai, C.-H.; Ashby, D.; Moz, M.; Gogotsi, Y.; Pilon, L.; Dunn, B. Designing Pseudocapacitance for Nb$_2$O$_5$/Carbide-Derived Carbon Electrodes and Hybrid Devices. *Langmuir* **2017**, *33* (37), 9407−9415.

(14) Reichman, B.; Bard, A. J. Electrochromism at Niobium Pentoxide Electrodes in Aqueous and Acetonitrile Solutions. *J. Electrochem. Soc.* **1980**, *127* (1), 241−242.

(15) Rolison, D. R.; Nazar, L. F. Electrochemical Energy Storage to Power the 21st Century. *MRS Bull.* **2011**, *36* (7), 486−493.

(16) Rani, R. A.; Zoolfakar, A. S.; O'Mullane, A. P.; Austin, M. W.; Kalantar-Zadeh, K. Thin Films and Nanostructures of Niobium Pentoxide: Fundamental Properties, Synthesis Methods and Applications. *J. Mater. Chem. A* **2014**, *2* (38), 15683−15703.

(17) Kim, H.; et al. Ordered-Mesoporous Nb2O5/Carbon Composite as a Sodium Insertion Material. *Nano Energy* **2015**, *16*, 62−70.

(18) Tong, Z.; Yang, R.; Wu, S.; Shen, D.; Jiao, T.; Zhang, K.; Zhang, W.; Lee, C.-S. Surface-Engineered Black Niobium Oxide@Graphene Nanosheets for High-Performance Sodium-/Potassium-Ion Full Batteries. *Small* **2019**, *15* (28), No. 1901272.

(19) Chen, Y.; Yousaf, M.; Wang, Y.; Wang, Z.; Lou, S.; Han, R. P. S.; Yang, Y.; Cao, A. Nanocable with Thick Active Intermediate Layer for Stable and High-Areal-Capacity Sodium Storage. *Nano Energy* **2020**, *78*, No. 105265.

(20) Subramanian, Y.; Veerasubramani, G. K.; Park, M.-S.; Kim, D.-W. Core-Shell Structured Nb2O5@N-Doped Carbon Nanoparticles as an Anode Material for Na-Ion Batteries. *Mater. Lett.* **2022**, *314*, No. 131891.

(21) Yan, L.; Chen, G.; Sarker, S.; Richins, S.; Wang, H.; Xu, W.; Rui, X.; Luo, H. Ultrafine Nb$_2$O$_5$ Nanocrystal Coating on Reduced Graphene Oxide as Anode Material for High Performance Sodium Ion Battery. *ACS Appl. Mater. Interfaces* **2016**, *8* (34), 22213−22219.

(22) She, L.; Yan, Z.; Kang, L.; He, X.; Lei, Z.; Shi, F.; Xu, H.; Sun, J.; Liu, Z.-H. Nb$_2$O$_5$ Nanoparticles Anchored on an N-Doped Graphene Hybrid Anode for a Sodium-Ion Capacitor with High Energy Density. *ACS Omega* **2018**, *3* (11), 15943−15951.

(23) Han, X.; Russo, P. A.; Triolo, C.; Santangelo, S.; Goubard-Bretesché, N.; Pinna, N. Comparing the Performance of Nb2O5 Composites with Reduced Graphene Oxide and Amorphous Carbon in Li- and Na-Ion Electrochemical Storage Devices. *ChemElectroChem.* **2020**, *7* (7), 1689−1698.

(24) Zhang, S.; Liu, G.; Qiao, W.; Wang, J.; Ling, L. Oxygen Vacancies Enhance the Lithium Ion Intercalation Pseudocapacitive Properties of Orthorhombic Niobium Pentoxide. *J. Colloid Interface Sci.* **2020**, *562*, 193−203.

(25) Shen, P.; Zhang, B.; Wang, Y.; Liu, X.; Yu, C.; Xu, T.; Mofarah, S. S.; Yu, Y.; Liu, Y.; Sun, H.; Arandiyan, H. Nanoscale Niobium Oxides Anode for Electrochemical Lithium and Sodium Storage: A Review of Recent Improvements. *J. Nanostruct Chem.* **2021**, *11* (1), 33−68.

(26) Wu, Y.; et al. Mesoporous Niobium Pentoxide/Carbon Composite Electrodes for Sodium-Ion Capacitors. *J. Power Sources* **2018**, *408*, 82−90.

(27) Miao, J.; Wu, M.; Li, X.; Ouyang, C.; Hong, Z.; Zhi, M. Molten Na Reduced T-Nb2O5 Nanorods Enable Enhanced Na-Storage Performance. *J. Phys. Chem. Solids* **2023**, *176*, No. 111235.

(28) Ni, J.; Wang, W.; Wu, C.; Liang, H.; Maier, J.; Yu, Y.; Li, L. Highly Reversible and Durable Na Storage in Niobium Pentoxide through Optimizing Structure, Composition, and Nanoarchitecture. *Adv. Mater.* **2017**, *29* (9), No. 1605607.

(29) Zhang, X. 3D Ordered Macroporous Amorphous Nb2O5 as Anode Material for High-Performance Sodium-Ion Batteries. *Appl. Surf. Sci.* **2021**, *567*, 150862.

(30) Nico, C.; Monteiro, T.; Graça, M. P. F. Niobium Oxides and Niobates Physical Properties: Review and Prospects. *Prog. Mater. Sci.* **2016**, *80*, 1−37.

(31) Barnes, P.; Zuo, Y.; Dixon, K.; Hou, D.; Lee, S.; Ma, Z.; Connell, J. G.; Zhou, H.; Deng, C.; Smith, K.; Gabriel, E.; Liu, Y.; Maryon, O. O.; Davis, P. H.; Zhu, H.; Du, Y.; Qi, J.; Zhu, Z.; Chen, C.; Zhu, Z.; Zhou, Y.; Simmonds, P. J.; Briggs, A. E.; Schwartz, D.; Ong, S. P.; Xiong, H. Electrochemically Induced Amorphous-to-Rock-Salt Phase Transformation in Niobium Oxide Electrode for Li-Ion Batteries. *Nat. Mater.* **2022**, *21*, 795.

(32) Barnes, P.; Savva, A.; Dixon, K.; Bull, H.; Rill, L.; Karsann, D.; Croft, S.; Schimpf, J.; Xiong, H. Electropolishing Valve Metals with a Sulfuric Acid-Methanol Electrolyte at Low Temperature. *Surf. Coat. Technol.* **2018**, *347*, 150−156.

(33) Lee, K.; Yang, Y.; Yang, M.; Schmuki, P. Formation of Highly Ordered Nanochannel Nb Oxide by Self-Organizing Anodization. *Chemistry − A European Journal* **2012**, *18* (31), 9521−9524.

(34) Scherrer, P. Bestimmung der Größe und der inneren Struktur von Kolloidteilchen mittels Röntgenstrahlen. *Nachrichten von der Gesellschaft der Wissenschaften zu Göttingen, Mathematisch-Physikalische Klasse* **1918**, *1918*, 98−100.

(35) Langford, J. I.; Wilson, A. J. C. Scherrer after Sixty Years: A Survey and Some New Results in the Determination of Crystallite Size. *J. Appl. Crystallogr.* **1978**, *11* (2), 102−113.

(36) Lindström, H.; Södergren, S.; Solbrand, A.; Rensmo, H.; Hjelm, J.; Hagfeldt, A.; Lindquist, S.-E. Li+ Ion Insertion in TiO2 (Anatase). 2. Voltammetry on Nanoporous Films. *J. Phys. Chem. B* **1997**, *101* (39), 7717−7722.

(37) Wang, J.; Polleux, J.; Lim, J.; Dunn, B. Pseudocapacitive Contributions to Electrochemical Energy Storage in TiO2 (Anatase) Nanoparticles. *J. Phys. Chem. C* **2007**, *111* (40), 14925−14931.

(38) Liu, T.-C.; Pell, W. G.; Conway, B. E.; Roberson, S. L. Behavior of Molybdenum Nitrides as Materials for Electrochemical Capacitors: Comparison with Ruthenium Oxide. *J. Electrochem. Soc.* **1998**, *145* (6), 1882.

(39) Weppner, W.; Huggins, R. A. Determination of the Kinetic Parameters of Mixed-Conducting Electrodes and Application to the System Li3Sb. *J. Electrochem. Soc.* **1977**, *124* (10), 1569−1578.